Targeted deletion of the gene encoding iron regulatory protein-2 causes misregulation of iron metabolism and neurodegenerative disease in mice

Timothy LaVaute[1], Sophia Smith[1], Sharon Cooperman[1], Kazuhiro Iwai[1], William Land[1], Esther Meyron-Holtz[1], Steven K. Drake[1], Georgina Miller[2], Mones Abu-Asab[3], Maria Tsokos[3], Robert Switzer III[4], Alexander Grinberg[5], Paul Love[5], Nancy Tresser[6] & Tracey A. Rouault[1]

In mammalian cells, regulation of the expression of proteins involved in iron metabolism is achieved through interactions of iron-sensing proteins known as iron regulatory proteins (IRPs), with transcripts that contain RNA stem-loop structures referred to as iron responsive elements (IREs). Two distinct but highly homologous proteins, IRP1 and IRP2, bind IREs with high affinity when cells are depleted of iron, inhibiting translation of some transcripts, such as ferritin, or turnover of others, such as the transferrin receptor (TFRC). IRPs sense cytosolic iron levels and modify expression of proteins involved in iron uptake, export and sequestration according to the needs of individual cells[1,2]. Here we generate mice with a targeted disruption of the gene encoding Irp2 (*Ireb2*). These mutant mice misregulate iron metabolism in the intestinal mucosa and the central nervous system. In adulthood, *Ireb2*^{−/−} mice develop a movement disorder characterized by ataxia, bradykinesia and tremor. Significant accumulations of iron in white matter tracts and nuclei throughout the brain precede the onset of neurodegeneration and movement disorder symptoms by many months. Ferric iron accumulates in the cytosol of neurons and oligodendrocytes in distinctive regions of the brain. Abnormal accumulations of ferritin colocalize with iron accumulations in populations of neurons that degenerate, and iron-laden oligodendrocytes accumulate ubiquitin-positive inclusions. Thus, misregulation of iron metabolism leads to neurodegenerative disease in *Ireb2*^{−/−} mice and may contribute to the pathogenesis of comparable human neurodegenerative diseases.

The two IRPs are simultaneously expressed in most mammalian tissues and cell lines, and transcripts that contain consensus IREs (such as ferritin) are well regulated by either IRP (ref. 3), indicating that IRP regulatory activities are potentially highly redundant. IRPs differ from one another in that IRE-binding activity of IRP1 is regulated primarily by reversible binding of a labile iron-sulfur cluster[1,2,4], whereas IRP2 activity is determined by its concentration, which depends on its rate of iron-dependent degradation[5,6] and transcription[7].

To evaluate the role of each Irp in regulation of iron homeostasis, we have generated mice with targeted disruptions of *Aco1* (also known as *Irp1*) or *Ireb2* (*Ireb2*[tm1Roua]). We report here on *Ireb2*^{−/−} mice, which were generated as described (Fig. 1*a–d*). In *Ireb2*^{−/−} embryonic fibroblasts, regulation of Irp1 binding activity was normal (Fig. 1*e*) and modulation of Tfrc and ferritin biosynthesis was similar to wild type (Fig. 1*f*), indicating that

sensing and regulation by Irp1 alone was sufficient to mediate regulation of several important iron metabolism proteins. *In situ* hybridization of 12.5-day-old embryos revealed that Irp2 was ubiquitously expressed, with highest levels in forebrain, hindbrain and spinal cord (Fig. 1*g*).

Ireb2^{−/−} mice initially grew and developed normally. *Ireb2*^{−/−} mice older than six months of age developed a progressive neurodegenerative disease characterized initially by an unsteady, wide-based gait and subtle kyphosis followed by the gradual onset of ataxia, vestibular dysfunction, tremor, bradykinesia and postural abnormalities (Fig. 1*h*). Balance and grip strength measured using the hanging wire test[8] indicated that *Ireb2*^{−/−} mice were severely impaired compared with wild type, whereas *Ireb2*^{+/−} mice showed an intermediate degree of impairment (Fig. 1*h*). Hematocrits, serum irons, transferrin, liver function tests, electrolytes, serum ceruloplasmins and creatine phosphokinase measurements of *Ireb2*^{−/−} mice were within the normal range. Serum ferritins were significantly elevated in 6- and 9-month *Ireb2*^{−/−} mice, and elevated in 12-month *Ireb2*^{−/−} mice (342 ± 25 ng/μl for wild-type mice compared with $1,295\pm189$ ng/μl for *Ireb2*^{−/−}). Tissue ashing revealed increased iron in liver and duodenal mucosa; total liver iron of 8-month wild-type mice was 947 ± 48 p.p.m. compared with $1,623\pm206$ p.p.m. for *Ireb2*^{−/−} mice and total duodenal mucosal iron of 8-month wild-type mice was 648 ± 51 p.p.m. compared with 968 ± 88 p.p.m. for *Ireb2*^{−/−} mice.

We detected increased ferric iron by Prussian blue staining in epithelial cells of the duodenal mucosa (Fig. 2*a,b*). To evaluate the potential molecular basis for ferric iron accumulation in the intestinal mucosa of *Ireb2*^{−/−} mice, we carried out immunohistochemistry using antibodies specific for ferritin, Tfrc, the apical ferrous iron transporter Dmt1 (ref. 9), and the basolateral iron transporter ferroportin-1 (ref. 10; also known as Ireg1 (ref. 11) and MTP1 (ref. 12)). Ferritin expression was increased in epithelial cells of the distal villi of *Ireb2*^{−/−} animals compared with controls (Fig. 2*c,d*). In addition, expression of two alternative splice forms of Dmt1 (Fig. 2*e–h*) and of the basolateral transporter (Fig. 2*i,j*) was increased in the same cells. Thus, the absence of Irp2 was associated with abnormally high expression levels of ferritin, together with increased expression of the apical and basolateral iron transport proteins that control the flux of iron across the duodenal mucosa. Comparison of the Prussian blue staining pattern with the ferritin staining pattern indicated that much of the detectable ferric iron was likely sequestered within ferritin.

[1]*Cell Biology and Metabolism Branch, National Institute of Child Health and Human Development, Bethesda, Maryland, USA.* [2]*Veterinary Resources Program, Office of the Director, National Institutes of Health, Bethesda, Maryland, USA.* [3]*Division of Clinical Sciences, National Cancer Institute, Bethesda, Maryland, USA.* [4]*NeuroScience Associates, Knoxville, Tennessee, USA.* [5]*Laboratory of Mammalian Genetics and Development, National Institute of Child Health and Human Development, Bethesda, Maryland, USA.* [6]*Neuroimmunology Branch, National Institute of Neurologic Disease and Stroke, Bethesda, Maryland, USA. Correspondence should be addressed to T.A.R. (e-mail: trou@helix.nih.gov).*

To evaluate the neuropathologic basis of the movement disorder, we carried out sequential sectioning and staining on brains of *Ireb2*^{−/−} and wild-type littermates of several different ages. Increased iron accumulation relative to age-matched wild-type controls was revealed by sensitive stains for ferric iron[13] in discrete regions of white and gray matter of *Ireb2*^{−/−} mice. Prominently affected areas included cerebellar white matter, caudate-putamen, thalamus and colliculi. Areas that were spared included the cerebral cortex and globus pallidus. Accumulation of iron was prominent in axonal elements of white matter tracts as well as in interfascicular oligodendrocytes (Fig. 3).

We detected axonal degeneration by staining with amino cupric silver reagent[14] in most of the white matter tracts that manifested iron accumulation. In cerebellar white matter of *Ireb2*^{−/−} mice, iron accumulated in axons and the somata of interfascicular oligodendrocytes (Fig. 4*c,d*). As evidenced by staining with amino cupric silver, sites of iron accumulation colocalized with sites of degeneration (Fig. 4*d,f*). Analysis of young mice

demonstrated that iron accumulation generally preceded axonal degeneration and accurately identified the sites of the CNS that would undergo neurodegeneration (data not shown).

Accumulation of iron in the cytoplasm of oligodendrocytes was a prominent feature in numerous white matter tracts throughout the brain of *Ireb2*^{−/−} mice (Fig. 4*g,h*). Although pathologic consequences of oligodendrocytic iron overload were not apparent on routine stains or ultrastructural analyses, we detected ubiquitin-containing inclusions in white matter tracts throughout the brain, particularly in cerebellar oligodendrocytes (Fig. 4*i,j*).

We detected iron accumulation in neuronal cell bodies in numerous gray matter areas, including portions of the thalamus, the deep cerebellar nuclei and colliculi (Fig. 5*b*). To evaluate the effect of iron accumulation in gray matter, areas rich in iron-laden neuronal cell bodies, including portions of the colliculi and thalamus, were prepared for ultrastructural evaluation[15]. Most neurons in these locations showed loss of nuclear membrane definition, shrinkage of nuclei and formation of cytoplasmic vacuoles (Fig. 5*d*).

Fig. 1 Generation and phenotype of *Ireb2*^{−/−} mice. *a*, A schematic diagram of the *Ireb2* genomic clone (top), *Ireb2*-mutant construct (middle), and *Ireb2*-mutant allele (bottom). *b*, Southern analysis of *Bam*HI digest of genomic DNA isolated from mouse tail cuts. The probe used for the genomic Southern blot was the 5′ *Bam*HI/*Sac*I fragment of the *Ireb2* genomic clone. In lane 1, wild-type genomic DNA shows a band of 15.1 kb; in lane 2, *Ireb2*^{+/−} genomic DNA shows a wild-type band of 15.1 kb and mutant band of 3.5 kb; in lane 3, *Ireb2*^{−/−} genomic DNA from a homozygous mutant shows only a band of 3.5 kb. Probing with neomycin confirmed a single 12-kb mutant allele (not shown). *c*, Northern-blot analysis of *Ireb2*. Total liver RNA (10 μg) from wild-type and *Ireb2*^{−/−} animals was probed with *Ireb2* cDNA. The 6.2-kb *Ireb2* transcript is absent from the *Ireb2*^{−/−} mouse, and a larger transcript containing the neomycin sequence and numerous in-frame stops was detected. *d*, Western-blot analysis of embryonic fibroblast cell lysates with antibodies specific for either Irp2 (top) or Irp1 (bottom) demonstrates absence of Irp2 from *Ireb2*^{−/−} lysates. *e*, Gel retardation assay of Irps. Lysates of wild-type and *Ireb2*^{−/−} mouse embryonic fibroblasts (5 μg) were incubated with ^{32}P-IRE and resolved on a 10% non-denaturing gel. Although the Irp2/IRE band shift activity is absent from lysates of *Ireb2*^{−/−} embryonic fibroblasts, the Irp1/IRE band shift activity (P1) seems to be normally regulated by the addition of either the iron chelator desferrioxamine (D) or the ferric ammonium citrate (F). *f*, Regulation of ferritin and Tfrc synthesis is normal in *Ireb2*^{−/−} embryonic fibroblasts after iron manipulations. Ferritin and Tfrc were quantitatively immunoprecipitated after radiolabeling and treatment with either an iron source (F-ferric ammonium sulfate 100 μg/ml) or an iron chelator (D-desferrioxamine 100 μg/ml) and wild-type ranges of regulation were observed in *Ireb2*^{−/−} cells. *g*, *In situ* hybridization of *Ireb2* in a 7-d embryo shows relatively high expression levels in forebrain (fb), hindbrain (hb) and spinal cord (sc). *Ireb2* is also detected in heart (h), liver (li), vertebrae (v), jaw (j), Rathke's pouch (rp), tongue (to), frontonasal mass (fm), genital eminence (ge) and intestine (i). Expression is detected in all tissues when anti-sense intensity (as) is compared with sense (s) controls. *h*, *Ireb2*^{−/−} mice at 12 months of age exhibit abnormal posture, poor grooming, piloerection and tremor. The eyes are often scarred and encrusted with purulent exudate and the tail is rigid and held erect. Many animals ambulate by walking unsteadily backwards. The gait is uncoordinated and jerky. The hind limbs are maintained in a flexed position and the abdomen rests on the ground. To quantitatively evaluate the movement disorder, balance and grip strength were measured using the hanging wire test[8] in *Ireb2*^{−/−}, *Ireb2*^{+/−} and wild-type mice that were matched by age and weight (30–35 g). In a 90-s test, wild-type mice averaged 87.14±2.85 s (n=7, average age 13 months), *Ireb2*^{+/−} mice averaged 55.62±9.08 s (n= 8, average age 12 months), and *Ireb2*^{−/−} mice averaged 21.45±4.96 s (n=11, average age 15 months).
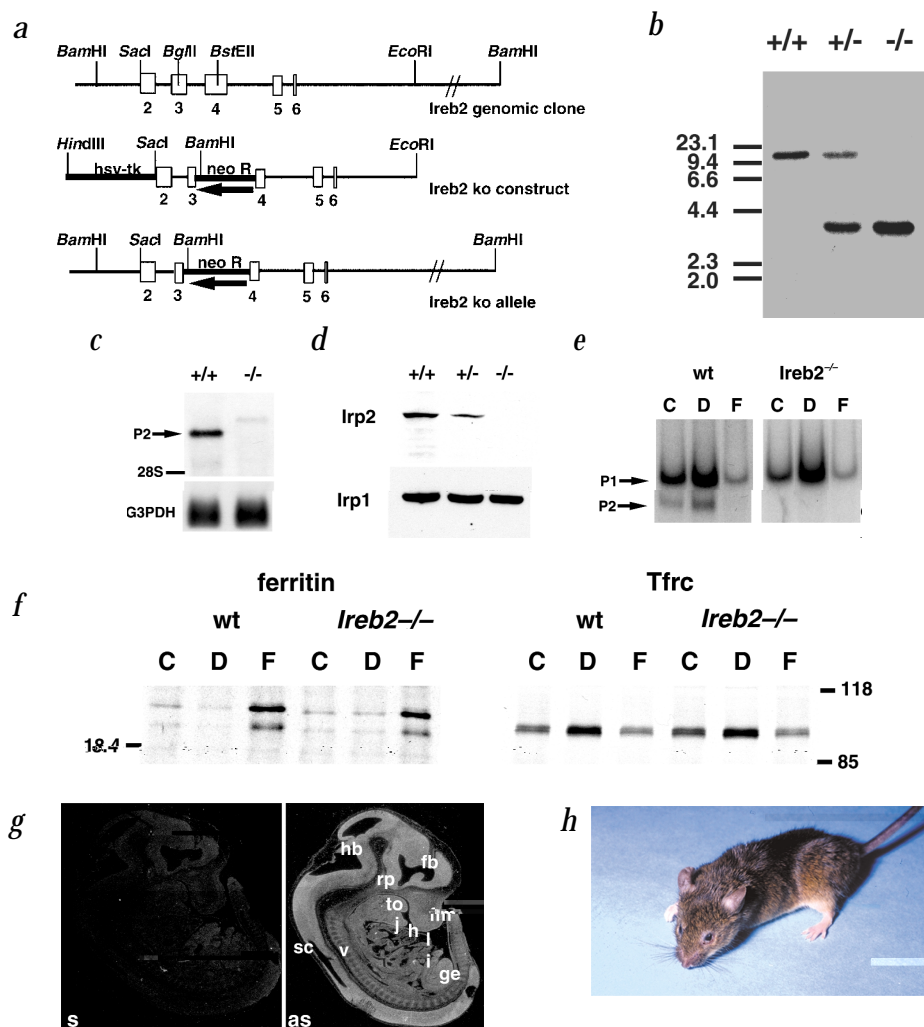
Fig. 2 Ferric iron accumulates in the duodenal mucosa of *Ireb2^{-/-}* mice, and expression levels of ferritin, both splice forms of Dmt1 and the basolateral iron exporter are high relative to controls on a normal diet. Prussian Blue staining is shown of duodenal mucosa from 4-month wild-type (***a***) and *Ireb2^{-/-}* littermates (***b***). Enterocytes near the tips of villi and macrophages of the lamina propria of the *Ireb2^{-/-}* mice stained positive for iron. A single villus is shown at higher magnification (see size bar) than the remainder of the figure to show the distribution of iron accumulation within cells. Ferritin expression (***c,d***) is comparable between wild-type and *Ireb2^{-/-}* mice in crypt epithelial cells, but is increased in the *Ireb2^{-/-}* epithelial cells distal to the crypt–villus junction. Mucous-secreting goblet cells do not show increased ferritin expression. Expression of two alternative splice forms of Dmt1 is increased in *Ireb2^{-/-}* mucosal epithelial cells. The two forms differ in the amino acid sequence of the carboxy terminus. The form labeled "IRE" contains a non-consensus IRE within the portion of the 3′ UTR encoded by an alternative exon (***e,f***), whereas the other splice form lacks an IRE (Dmt1 non-IRE) (***g,h***). Immunohistochemical detection of the basolateral transporter (ferroportin-1) in duodenal mucosa of wild-type (***i***) or *Ireb2^{-/-}* (***j***) mice reveals an increase in expression of the basolateral transporter in *Ireb2^{-/-}* mice. The size bar at bottom right indicates magnification for (***c–j***).
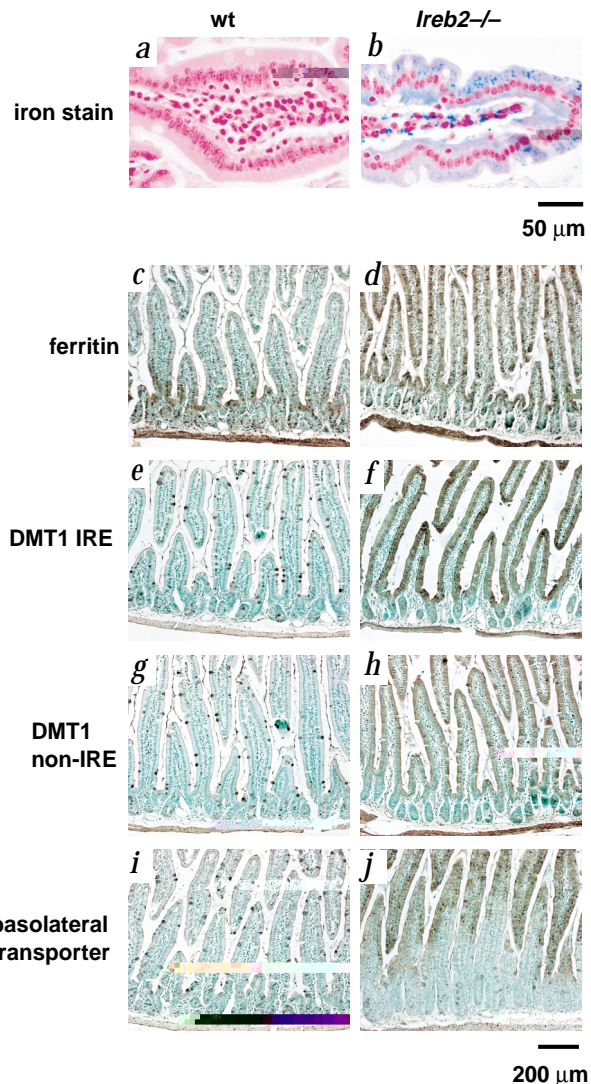
To further evaluate the basis for accumulation of excess cerebellar iron and its pathologic consequences, we established the identity of affected cells using cell-specific antibodies and compared the pattern of iron staining with that of ferritin expression. Increased ferritin expression throughout Purkinje axons (Fig. 6*b,d*) colocalized with marked accumulations of iron (Fig. 6*f,j*, inset). There was partial Purkinje cell loss in *Ireb2^{-/-}* animals, and ultrastructural evidence of degeneration was detected in many of the remaining Purkinje cells (Fig. 6*h,j*). In cerebellar lysates, expression of ferritin was increased, whereas Tfrc expression was decreased (Fig. 6*k*).

Overexpression of ferritin was a prominent feature in tissues that were adversely affected by genetic ablation of *Ireb2*. We propose that the cells most affected by loss of Irp2, including intestinal epithelium and neurons, are those in which Irp2 contributes a
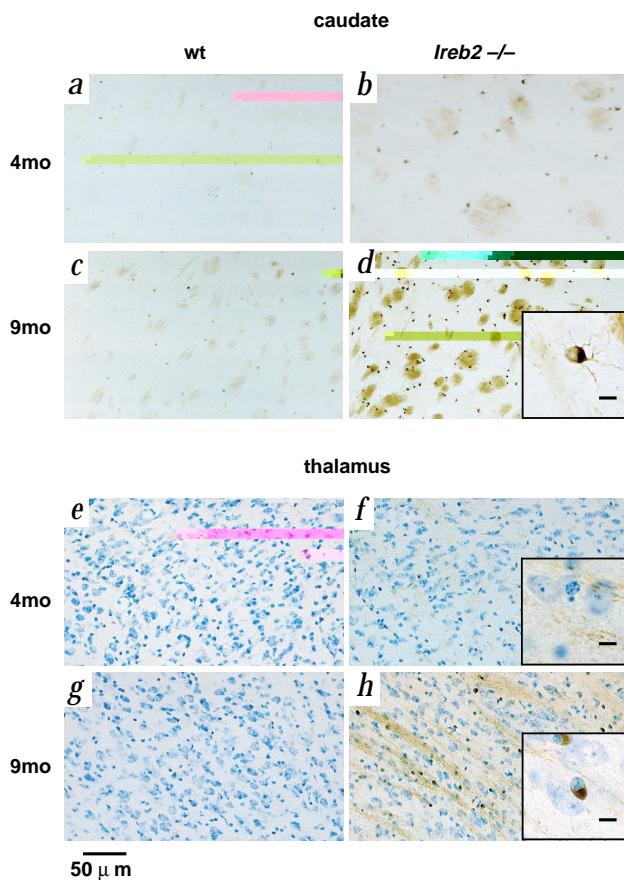
high proportion of total Irp activity[16] (T.L., unpublished data). Genetic ablation of *Ireb2* in highly Irp2-dependent cells may result in the loss of sufficient IRE binding activity to regulate the multiple targets of the IRP regulatory system. Functional IREs are found in the 5′ UTRs of transcripts encoding ferritin H and L chains[1,2], the ferroportin-1 transcript[12], the 3′ UTR of the Tfrc transcript (refs. 1,2) and one splice form of Dmt1 (ref. 9). Thus, loss of Irp2 may result in an inability to repress translation of transcripts encoding ferritin H and L chains and the basolateral transporter, along with an inability to protect the Tfrc transcript from degradation. A potential consequence of ferritin and ferroportin-1 overexpression would be functional iron deficiency. Overexpression of ferritin H-chain causes cytosolic iron depletion by

Fig. 3 Iron accumulates in white matter tracts of the caudate-putamen and thalamus in *Ireb2^{-/-}* mice and increases with age. In the caudate-putamen (***a–d***), iron was present in axon bundles and in oligodendrocytic cell bodies and processes (***d***, inset). Mild iron accumulation was also seen in older wild-type littermates (***c***). In the thalamus (***e–h***), iron accumulation was initially most prominent in axons (***f***, inset) and accumulation of iron in oligodendrocytes (***h***, inset) occurred later. Axonal iron (***f***, inset) was present in 4-month animals, but degeneration did not become appreciable until animals were many months older (not shown). Size bars of insets, 10 μm. Iron accumulation characteristically increased with age in specific brain areas in both wild-type and *Ireb2^{-/-}* mice, but *Ireb2^{-/-}* mice consistently accumulated more iron than age-matched controls (***a–h***). Staining with Luxol fast blue for myelin revealed that the accumulated iron was present in axons rather than in the myelin sheath (not shown).
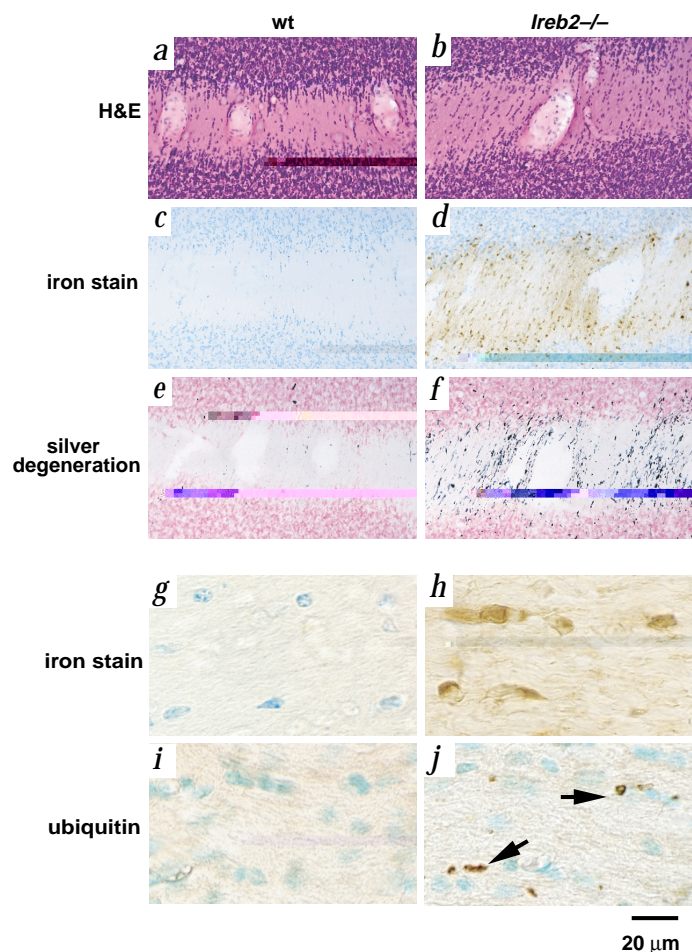
Fig. 4 Iron accumulation and axonal degeneration colocalize in the cerebellar white matter of *Ireb2⁻/⁻* mice and cerebellar oligodendrocytes of *Ireb2⁻/⁻* mice accumulate cytosolic iron and form ubiquitin inclusions. Sequential coronal sections of cerebellar vermis from littermates stained with hematoxylin and eosin (H&E; *a,b*), Perls' DAB iron stain (*c,d*) or amino cupric silver (*e,f*) are shown (photographed with ×20 objective). A blood vessel in (*d*) and (*f*) aids in aligning sequential sections. Iron accumulations within axons appear as thread-like vertical lines, and darker intensely stained spots are oligodendrocytes that contain cytosolic iron (shown at higher magnification in *h*). Interfascicular oligodendrocytes appear in rows in cerebellar white matter. The nuclei are counterstained with methyl green (*g–j*) and the identity of these cells has been confirmed by staining with CNPase, an oligodendrocyte marker (not shown). Iron accumulations within the cytosol of oligodendrocytes are flame or sickle-shaped and many of the nuclei are eccentrically located (*h*). Ubiquitin inclusions (dark brown punctate spots indicated by arrowheads) appear in rows in cerebellar white matter in *Ireb2⁻/⁻* mice (*j*), and ubiquitin staining colocalizes with staining for oligodendrocyte cytosol (not shown).

Methods

Targeted deletion of *Ireb2*. Embryonic stem cells were transfected with an *Ireb2*-mutant construct made using a genomic *Ireb2* clone derived from a 129/Sv library and the targeting vector pPNT (ref. 18). We subcloned a 1.8-kb *Sst*I (blunted)-*Bgl*II fragment of the *Ireb2* clone, containing parts of exons 2 and 3, into the *Eco*RI (blunted)-*Bam*HI sites of pPNT, generating the 5′ arm of the construct. The 3′ arm was generated by subcloning a 6.6-kb *Bst*EII-*Eco*RI fragment of the *Ireb2* genomic clone (which contains part of exon 4 and exons 5 and 6). This fragment was fitted with *Xho*I and *Not*I linkers and subcloned into the *Xho*I and *Not*I sites of pPNT. The targeting construct was linearized with *Not*I before electroporation into ES cells[18]. Chimeric mice were bred, back-crossed to C57Bl/6 mice and genotyped[18]. We carried out northern-blot analysis[19] using the complete *Ireb2* cDNA as a probe.

Generation of embryonic fibroblasts, gel retardation assays and immunoprecipitations. Embryonic fibroblasts of 16-d embryos were isolated as described[20]. We carried out gel retardation assays[21] and ferritin and TFRC immunoprecipitations as described[22].

promoting oxidation and sequestration of cytosolic iron at the expense of other proteins[17]. Further cytosolic iron losses may be mediated by increased exporter expression, and a compensatory increase in expression of Tfrc would not be expected because of Irp insufficiency[1,2]. The unexplained increases in expression of Dmt1 isoforms may represent an Irp-independent response to functional iron deficiency.

Although selective neuronal vulnerability is characteristic of neurodegenerative disease, the basis for selectivity is rarely understood. In *Ireb2⁻/⁻* mice, misregulation of iron metabolism in affected neurons is implicated as a cause of neurodegeneration. The fact that *Ireb2⁺/⁻* mice develop a milder and later-onset form of the disease increases the possibility that human counterparts will be found. Evaluation of *Ireb2⁻/⁻* may promote understanding of the pathophysiology and treatment of neurodegenerative disease.

Fig. 5 Neuronal iron accumulation is associated with ultrastructural evidence of neurodegeneration in *Ireb2⁻/⁻* mice. Perls' DAB stains of the colliculi of 9-month littermates revealed increased accumulation of ferric iron in neuronal cytosol (*a,b*). Corresponding regions of the colliculi from 10-month animals were prepared for ultrastructural analysis and representative cells were photographed (*c,d*). In the *Ireb2⁻/⁻* brain sample, loss of definition of the nuclear membrane (in the nucleus labeled N) along with contraction and condensation of the nucleus and vacuolization of the cytosol (*d*, arrow) were features of most neuronal cell bodies examined. A single nucleus (N) is labeled in (*c*) and (*d*). Inset bar for (*a*) and (*b*), 10 μm. Many of the axons in these regions were distended (not shown) and the surrounding neuropil was disorganized and vacuolated; however, there was no increase in microglial staining and only minimal changes were observed in glial fibrillary acidic protein (GFAP) stains (a method for assessment of astrocyte activation) in 12-month *Ireb2⁻/⁻* animals (data not shown).
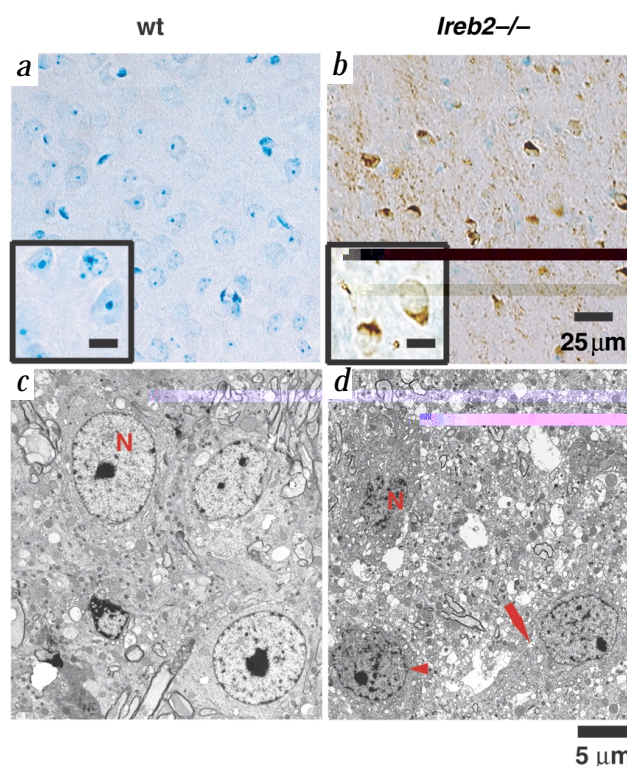
Fig. 6 Purkinje cells degenerate in *Ireb2*⁻/⁻ mice and increased Purkinje axonal ferritin expression colocalizes with increased iron accumulation in *Ireb2*⁻/⁻ mice. Cerebellar folia (sagittal sections) show increased ferritin staining (***b***) in the axons of *Ireb2*⁻/⁻ Purkinje cells. A red arrowhead points to increased ferritin in a Purkinje axon hillock, and a red arrow points to ferritin accumulations in numerous Purkinje axons in the white matter. Enlargements of the areas indicated by arrows in (***a***) and (***b***) are shown in (***c***) and (***d***). Increased iron accumulation detected by Perls' DAB iron staining of comparable sagittal sections indicates that iron accumulation is present in the extended axons of *Ireb2*⁻/⁻ Purkinje cells (***f***). The black arrow points to the region of the folium that corresponds to the area indicated by the red arrow in (***b***). An arrowhead indicates an iron-loaded oligodendrocyte (***f***). Purkinje cells (P) from 9-month wild-type and *Ireb2*⁻/⁻ littermates were stained with anti-calbindin antibody in coronal sections of

cerebellar vermis (***g,h***). The molecular (M) and granule cell layers (G) are labeled for orientation (***g***). Purkinje dendritic trees and axons were atrophic and loss of cell bodies was apparent in *Ireb2*⁻/⁻ mice, particularly at the tips of the cerebellar folia. Ultrastructural analysis of wild-type and *Ireb2*⁻/⁻ Purkinje cells revealed vacuolation, atrophy and loss of nuclear membrane integrity (***i,j***). A Purkinje cell from an 18-month *Ireb2*⁻/⁻ mouse stained with Perls' DAB and counterstained with luxol fast blue is shown in the inset of (***j***) (inset size bar, 10 μm). The arrowhead points to axonal iron that is characteristic of Purkinje cells of *Ireb2*⁻/⁻ mice, as shown at lower magnification in (***f***). A representative western blot of cerebellar lysates from 9-month littermates of different genotypes indicates that expression of ferritin is increased approximately fivefold in *Ireb2*⁻/⁻ compared with age-matched littermates, whereas Tfrc levels are approximately fourfold decreased, and levels of expression are intermediate in *Ireb2*⁺/⁻ animals (***k***). Ferritin levels progressively increase as *Ireb2*⁻/⁻ animals age, whereas Tfrc levels progressively decrease (not shown).
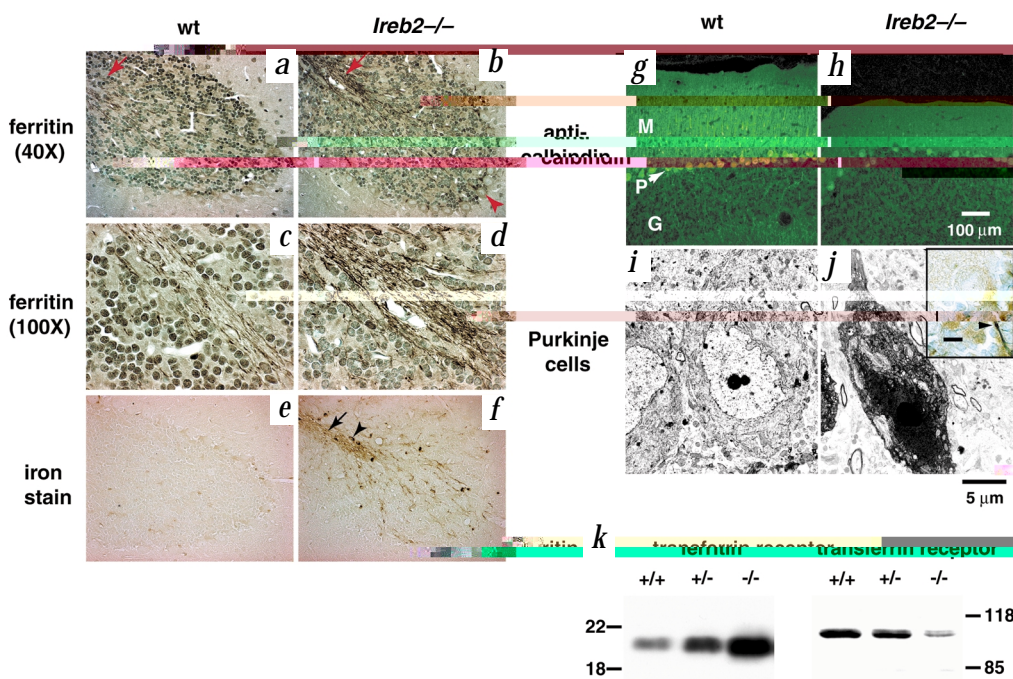
Chemistries and blood work. Complete blood counts were performed by Analytics, serum chemistries, by the Clinical Chemistry Service of the NIH, and serum ceruloplasmin analyses, by J. Gitlin. Tissue iron analyses were performed by the Chemical Analysis Laboratory at the University of Georgia in accordance with EPA method 6010.

Serum ferritin assays. We measured serum ferritin by colorigenic ELISA essentially as described for human ferritin[23]. Reaction product from the reaction substrate, chlorophenol red β-D-galactopyranoside (CPRG), was measured with the ELISA spectrocolorimeter MR5000 (Dynatech Laboratories) using a primary filter with a peak transmission at 570 nm and a second filter with a transmission at 620 nm.

Western-blot analysis. We detected Irp2 using a polyclonal antibody raised in rabbits against aa 137–209 of the human IRP2 sequence, over-expressed and purified from *Escherichia coli* as described[19]. We detected ferritin using rabbit anti-sera to mouse ferritin at a dilution of 1:2,000, followed by ¹²⁵I-donkey anti-rabbit IgG (0.5 μCi/ml; Amersham Life Science). Tfrc was detected using a mouse monoclonal anti-Tfrc amino-terminus antibody (1 μg/ml; Zymed), followed by ¹²⁵I-sheep anti-mouse IgG (0.5 μCi/ml; Amersham Life Science).

Prussian blue staining of intestinal mucosa. Duodenum immediately distal to the pyloric ostium (1 cm) was fixed in formalin and embedded in paraffin. Cross-sections (7 μm) were stained with the Mallory method of Prussian blue staining, mixing 2.5% potassium ferrocyanide with 2.5% HCl for 20 min at RT, followed by rinsing with H_2O and counterstaining with nuclear fast red.

Immunohistochemistry of the intestinal mucosa. Anti-MAP (ref. 24) antibodies were raised in rabbits to peptides that correspond to carboxy termini encoded by two alternative splice forms of mouse Dmt1, one by an exon that contains a non-consensus IRE in the 3´ UTR (C-terminus-KVL LSEDTSG GNIK) and the other by an exon that lacks an IRE (C-terminus-QPELYLL

NTVDADSVVSR). Antibodies were also raised against a peptide from the mouse ferroportin sequence, aa 240–258 (KVEESELKQLTSPKDTEPK). Anti-MAP antibodies were affinity purified using affinity chromatography columns made by coupling the MAP antigen to cyanogen-bromide–activated Sepharose CL-4B. We used purified anti-MAP antibodies (1 μg/ml for detection of ferroportin and 10 μg/ml for detection of each alternative splice form of DMT1) to probe formalin-fixed, paraffin-embedded tissue. Pooled rabbit IgGs (5 μg/ml) were used as a negative control. We used goat anti-rabbit IgG conjugated to biotin as the secondary antibody in all cases (Vector Laboratories), followed by Avidin Biotin Complex labeled with horseradish peroxidase (ABC Elite kit, Vector Laboratories). HRP was visualized using the substrate diaminobenzidine (DAB, Vector Laboratories) with incubation for 5 min at RT. Ferritin immunohistochemistry was performed using prediluted ferritin antibody (Biogenesis) per the manufacturer's recommendations.

Brain histopathology. Mice of various genotypes and ages were perfused, gelatin-embedded brains were sectioned[25] and sequential sections were stained with hematoxylin and eosin for morphology, Perls'/DAB stain for ferric iron[13], and amino cupric silver stain for detection of degenerating axons[26]. Purkinje cells were detected with calbindin monoclonal antibody (CL300 Sigma) used at 1:1,000, followed by goat anti-mouse Alexa TM 488 (Molecular Probes) used at 1:2,000 and visualized by laser scanning confocal microscopy[27]. For oligodendrocyte identification, sections were probed with CNPase as described[28]. We detected ubiquitin inclusions as described[29] with primary antibody at 1:500 (Dako) in free-floating sections. Tissues for ultrastructural analyses were processed as described[15].

***In situ* hybridization.** We carried out *in situ* hybridization on 12.5-day embryos as described[30] by Phylogenetics, using sense and antisense probes from the first 704 bases (starting at the ATG) of the rat *Ireb2* cDNA, cloned into the *Sac*I site of pBlueScript KS (Stratagene).

GenBank accession numbers. Mouse Dmt1 with IRE, AAC24496.1, without IRE, P49282; mouse ferroportin-1, AAF36696.1.

letter

1. Rouault, T. & Klausner, R. Regulation of iron metabolism in eukaryotes. *Curr. Top. Cell Regul.* **35**, 1–19 (1997).
2. Hentze, M.W. & Kuhn, L.C. Molecular control of vertebrate iron metabolism: mRNA-based regulatory circuits operated by iron, nitric oxide, and oxidative stress. *Proc. Natl. Acad. Sci. USA* **93**, 8175–8182 (1996).
3. Kim, H.Y., Klausner, R.D. & Rouault, T.A. Translational repressor activity is equivalent and is quantitatively predicted by in vitro RNA binding for two iron-responsive element binding proteins, IRP1 and IRP2. *J. Biol. Chem.* **270**, 4983–4986 (1995).
4. Beinert, H., Kennedy, M.C. & Stout, D.C. Aconitase as iron-sulfur protein, enzyme, and iron-regulatory protein. *Chem. Rev.* **96**, 2335–2373 (1996).
5. Guo, B., Phillips, J.D., Yu, Y. & Leibold, E.A. Iron regulates the intracellular degradation of iron regulatory protein 2 by the proteasome. *J. Biol. Chem.* **270**, 21645–21651 (1995).
6. Iwai, K. *et al.* A. Iron-dependent oxidation, ubiquitination, and degradation of iron regulatory protein 2: implications for degradation of oxidized proteins. *Proc. Natl. Acad. Sci. USA* **95**, 4924–4928 (1998).
7. Wu, K.J., Polack, A. & Dalla-Favera, R. Coordinated regulation of iron-controlling genes, H-ferritin and IRP2, by c-MYC. *Science* **283**, 676–679 (1999).
8. Sango, K. *et al.* Mice lacking both subunits of lysosomal β-hexosaminidase display gangliosidosis and mucopolysaccharidosis. *Nature Genet.* **14**, 348–352 (1996).
9. Andrews, N.C., Fleming, M.D. & Gunshin, H. Iron transport across biologic membranes. *Nutr. Rev.* **57**, 114–123 (1999).
10. Donovan, A. *et al.* Positional cloning of zebrafish ferroportin1 identifies a conserved vertebrate iron exporter. *Nature* **403**, 776–781 (2000).
11. McKie, A.T. *et al.* A novel duodenal iron-regulated transporter, IREG1, implicated in the basolateral transfer of iron to the circulation. *Mol. Cell* **5**, 299–309 (2000).
12. Abboud, S. & Haile, D.J. A novel mammalian iron-regulated protein involved in intracellular iron metabolism. *J. Biol. Chem.* **275**, 19906–19912 (2000).
13. Francois, C., Nguyen-Legros, J. & Percheron, G. Topographical and cytological localization of iron in rat and monkey brains. *Brain Res.* **215**, 317–322 (1981).
14. de Olmos, J.S., Beltramino, C.A. & de Olmos de Lorenzo, S. Use of an amino-cupric-silver technique for the detection of early and semiacute neuronal degeneration caused by neurotoxicants, hypoxia, and physical trauma. *Neurotoxicol. Teratol.* **16**, 545–561 (1994).
15. Katz, R.L. *et al.* An intra-abdominal small round cell neoplasm with features of primitive neuroectodermal and desmoplastic round cell tumor and a EWS/FLI-1 fusion transcript. *Hum. Pathol.* **28**, 502–509 (1997).
16. Henderson, B.R., Seiser, C. & Kuhn, L.C. Characterization of a second RNA-binding protein in rodents with specificity for iron-responsive elements. *J. Biol. Chem.* **268**, 27327–27334 (1993).
17. Cozzi, A. *et al.* Overexpression of wild type and mutated human ferritin H-chain in HeLa cells: in vivo role of ferritin ferroxidase activity. *J. Biol. Chem.* **275**, 25122–25129 (2000).
18. Love, P.E. *et al.* T cell development in mice that lack the zeta chain of the T cell antigen receptor complex. *Science* **261**, 918–921 (1993).
19. Kim, H.Y., LaVaute, T., Iwai, K., Klausner, R.D. & Rouault, T.A. Identification of a conserved and functional iron-responsive element in the 5′ UTR of mammalian mitochondrial aconitase. *J. Biol. Chem.* **271**, 24226–24230 (1996).
20. Ishino, K., Kaneyama, J., Shibanuma, M. & Nose, K. Specific decrease in the level of Hic-5, a focal adhesion protein, during immortalization of mouse embryonic fibroblasts, and its association with focal adhesion kinase. *J. Cell. Biochem.* **76**, 411–419 (2000).
21. Allerson, C.R., Cazzola, M. & Rouault, T.A. Clinical severity and thermodynamic effects of iron-responsive element mutations in hereditary hyperferritinemia-cataract syndrome. *J. Biol. Chem.* **274**, 26439–26447 (1999).
22. DeRusso, P.A. *et al.* Expression of a constitutive mutant of iron regulatory protein 1 abolishes iron homeostasis in mammalian cells. *J. Biol. Chem.* **270**, 15451–15454 (1995).
23. Konijn, A.M., Levy, R., Link, G. & Hershko, C. A rapid and sensitive ELISA for serum ferritin employing a fluorogenic substrate. *J. Immunol. Methods* **54**, 297–307 (1982).
24. Tam, J.P. Synthetic peptide vaccine design: synthesis and properties of a high-density multiple antigenic peptide system. *Proc. Natl. Acad. Sci. USA* **85**, 5409–5413 (1988).
25. Fix, A.S. & Garman, R.H. Practical aspects of neuropathology: a technical guide for working with the nervous system. *Toxicol. Pathol.* **28**, 122–131 (2000).
26. Fix, A.S., Ross, J.F., Stitzel, S.R. & Switzer, R.C. Integrated evaluation of central nervous system lesions: stains for neurons, astrocytes, and microglia reveal the spatial and temporal features of MK-801-induced neuronal necrosis in the rat cerebral cortex. *Toxicol. Pathol.* **24**, 291–304 (1996).
27. Ellenberg, J. *et al.* Nuclear membrane dynamics and reassembly in living cells: targeting of an inner nuclear membrane protein in interphase and mitosis. *J. Cell Biol.* **138**, 1193–1206 (1997).
28. Yin, X., Peterson, J., Gravel, M., Braun, P.E. & Trapp, B.D. CNP overexpression induces aberrant oligodendrocyte membranes and inhibits MBP accumulation and myelin compaction. *J. Neurosci. Res.* **50**, 238–247 (1997).
29. Arai, N., Papp, M.I. & Lantos, P.L. New observation on ubiquitinated neurons in the cerebral cortex of multiple system atrophy (MSA). *Neurosci. Lett.* **182**, 197–200 (1994).
30. Lyons, G.E., Schiaffino, S., Sassoon, D., Barton, P. & Buckingham, M. Developmental regulation of myosin gene expression in mouse cardiac muscle. *J. Cell Biol.* **111**, 2427–2436 (1990).